Extreme events and instantons in Lagrangian passive scalar turbulence models

Mnerh Alqahtani [1,*] Leonardo Grigorio [2] and Tobias Grafke [1]
[1]*Mathematics Institute, University of Warwick, Coventry CV4 7AL, United Kingdom*
[2]*Centro Federal de Educação Tecnológica Celso Suckow da Fonseca, 28635-000, Nova Friburgo, RJ, Brazil*

(Received 4 August 2021; revised 23 November 2021; accepted 22 April 2022; published 1 July 2022)

The advection and mixing of a scalar quantity by fluid flow is an important problem in engineering and natural sciences. The statistics of the passive scalar exhibit complex behavior even in the presence of a Gaussian velocity field. This paper is concerned with two Lagrangian turbulence models that are based on the recent fluid deformation model, but adding a passive scalar field with uniform mean gradient. For a range of Reynolds numbers, these models can reproduce the statistics of passive scalar turbulence. For these models, we demonstrate how events of extreme passive scalar gradients can be recovered by computing the instanton, i.e., the saddle-point configuration of the associated stochastic field theory. It allows us to both reproduce the heavy-tailed statistics associated with passive scalar turbulence, and recover the most likely mechanism leading to such extreme events. We further demonstrate that events of large negative strain in these models undergo spontaneous symmetry breaking.

DOI: 10.1103/PhysRevE.106.015101

I. INTRODUCTION

The 3D incompressible *Navier-Stokes equations* (NSE),

$$\partial_t u + u \cdot \nabla u + \nabla p - \nu \Delta u = 0, \qquad \nabla \cdot u = 0, \qquad (1)$$

describe the evolution of a fluid in time. Here, $u(x,t) \in \mathbb{R}^3$ is the velocity field, ν denotes the kinematic viscosity, and $p(x,t) \in \mathbb{R}$ is the scalar pressure field that enforces the incompressibility constraint. A passive scalar, such as a substance concentration (e.g., pollutant or temperature field without buoyancy feedback), is advected by a turbulent flow exhibiting complex spatial and temporal scales of motions. The *passive scalar equation* (PSE) gives its time evolution,

$$\partial_t \theta + u \cdot \nabla \theta - \kappa \, \Delta \theta = 0, \qquad (2)$$

where κ denotes the diffusivity coefficient of $\theta(x,t) \in \mathbb{R}$. Passive scalar turbulence is often taken as a testbed for understanding fluid turbulence [1,2], but is also relevant in its own right to analyze, for example, advection processes in the atmosphere [3,4] or ocean [5,6].

Understanding the statistical and geometrical properties of turbulent flow at small scales has been a long-standing challenge. At these scales of motion, the prolific activity of strain and vorticity triggers intense fluctuations, resulting in *intermittency*, as observed in the probability distribution functions (PDFs) of velocity gradients [7]. The velocity gradient not only dominates the smallest scales of motion, but it also embodies local rotation and deformation rate, making it an observable object of theoretical [8–10] and numerical/experimental studies [11–13]. The dynamics of small inertial particles immersed in a turbulent flow is dictated by the flow velocity gradients [14–16]. The small-scale statistics of passive scalar fluctuations have sparked the same level of curiosity, as the scalar field displays anomalous scaling even in a completely Gaussian velocity field [17,18]. Other scalar turbulence features have been studied such as the rise of large-scale anisotropic scalar structures regardless of Reynolds number [19], the inefficiency of turbulent flow mixing linked to a high Schmidt number [20], anomalous scaling [21], and statistical moments [22,23].

Aiming at obtaining the statistics of the small scales provided by the velocity gradients $A_{ij} = \partial u_i / \partial x_j$, a variety of low dimensional models has been proposed in the literature describing the evolution of A_{ij} following a tracer particle (Lagrangian description). As the effect of pressure and viscosity renders the dynamical equation for A_{ij} unclosed, one is forced to resort to some closure approximation to obtain a self-contained model [24]. The *restricted Euler* (RE) equation [8], the *tetrad model* [25], and the *recent fluid deformation* (RFD) [26] form a history of such models, where in particular the last has successfully regularized the finite-time singularity of the nonlinear self-stretching term $(-\mathbb{A}^2)$ observed in the RE model, using ideas from linear damping [24,27] and geometrical considerations of Ref. [25]. At the same time, it preserves the statistical features of the velocity gradient such as the left-skewness of its distribution, and the properties of the joint PDFs in the Q-R plane, where Q and R are the second and third invariants of $\mathbb{A}$, respectively. Nevertheless, the RFD model is restricted to moderate Reynolds numbers.

Reframing the closure problem in terms of conditional averages, Ref. [28] proposes a model for the velocity gradient by closing the deviatoric pressure Hessian and viscous Laplacian conditional means with the help of a Gaussian velocity field. Evaluation of the Gaussian conditional averages allows for an analytical estimation of the model parameters. However, the resulting model suffers from singularities when computed numerically. This issue has been circumvented with an empirical adjustment of parameters, retaining the functional form

*Corresponding author: M.Alqahtani@warwick.ac.uk

of the Gaussian approximation, and resulting in the enhanced Gaussian fields (EGF) closure. More recently, Ref. [29] merges the two approaches, viz. the RFD and EGF, into a model called RDGF (recent deformation Gaussian fields), taking advantage of both closures. In an attempt to extend RFD closure to any Reynolds numbers, [30] proposes a model that constrains the dynamics, such that the dissipation fulfils certain statistical features at the cost of introducing another free parameter that controls the intermittency.

The Lagrangian evolution of a passive scalar can be added alongside the velocity gradient with similar arguments as for the RFD model. The resulting passive scalar RFD model (PS-RFD) proposed in Ref. [31] retains the statistical properties of the scalar gradient $\psi := \nabla\theta$, such as the fat-tailed PDFs of ψ deviating from Gaussian at small scales, in excellent agreement with full direct numerical simulations of passive scalar turbulence [32]. Extreme values of the scalar gradient dominate the tails, resulting in heavy-tailed distributions. These outlier large gradients of the passive scalar, prevailing at the inertial scales (intermittency), can effectively be studied by means of *instanton calculus* due to their low probabilities, which forms the main contribution of this work.

As we will line out below, the instanton formalism [33–35], and its more rigorous cousin, large deviation theory [36,37], rely on the fact that in stochastic systems, rare events often occur in a rather predictable way: While common events usually have a multitude of possible histories, outlier events must rely on a very precise interplay of physical mechanisms and forcing realizations, leading to a prototypical system trajectory for the desired rare event. At its core lies the estimation of a stochastic (path-)integral by a saddle-point approximation, or equivalently by a (functional) Laplace method, that computes the most likely trajectory, called the *instanton*, as well as its probability, as the solution of a large optimization problem. Instanton calculus has been successfully applied to many stochastic systems, including in fluid dynamics [38–41] and waves [42,43]. These principles will be applied in this paper to analyze outlier events in passive scalar turbulence. More specifically, we will investigate extreme gradients of θ for the PS-RFD models via the instanton formalism to find the most likely realization leading to outlier events, and compare the probability scaling predicted by the instanton to the observed heavy-tailed distribution of Monte Carlo (MC) simulations. This demonstrates how the instanton gives us direct access to the tail scaling of passive scalar turbulence.

This paper is structured as follows: Sec. II provides a brief overview of the RFD models of the flow velocity gradient and the passive scalar gradient. Following that, in Sec. III, we introduce a reduced version, based on axial and reflection symmetry considerations that are obeyed statistically by the system. We will investigate the limitations of these symmetry assumptions and the symmetry breaking of large strain events in Sec. III B. Section IV is devoted to the instanton formalism as applied to the PS-RFD system, including its action/rate function and a system of instanton equations that solve the optimization problem. Section V then analyzes heavy-tailed PDFs of the passive scalar gradient. Such heavy-tailed distributions, associated with nonconvex rate-functions, pose a particular difficulty for the application of sample-path large deviations; thus, we apply in Sec. V B a revised formalism based on nonlinear convexification of extreme event instantons [44]. Finally, we conclude in Sec. VI.

II. THE RECENT FLUID DEFORMATION MODELS

In this section, we briefly recall the recent fluid deformation model [26] and its extension to the dynamics of passive scalar gradients [31].

A. Lagrangian velocity gradient in the recent fluid deformation model

The Lagrangian time evolution of the velocity gradient tensor $\mathbb{A}$ is obtained by taking the gradient of the NSE (1):

$$\frac{dA_{ij}}{dt} = -A_{in}A_{nj} - \frac{\partial^2 p}{\partial x_i \partial x_j} + \nu \frac{\partial^2 A_{ij}}{\partial x_n \partial x_n}, \tag{3}$$

where $d/dt = \partial/\partial t + u_k\,\partial/\partial x_k$ stands for the material derivative. Due to the incompressibility of the flow, $\mathbb{A}$ must be traceless, $\mathrm{Tr}(\mathbb{A}) = 0$. As previously stated, Eq. (3) is not closed in terms of $\mathbb{A}$ at position x and time t because the anisotropic part of the pressure Hessian is highly nonlocal, and the Laplacian of $\mathbb{A}$ in the viscous term is not easily expressed in terms of $\mathbb{A}$.

The RFD closure models these unclosed terms based on the hypotheses detailed in Ref. [26]. The RFD dynamics of the deformation that the Lagrangian particle undergoes along the flow, Eq. (3), is

$$d\mathbb{A} = \left(-\mathbb{A}^2 + \frac{\mathrm{Tr}(\mathbb{A}^2)}{\mathrm{Tr}(\mathbb{C}^{-1})}\,\mathbb{C}^{-1} - \frac{\mathrm{Tr}(\mathbb{C}^{-1})}{3T}\mathbb{A}\right) dt + \sqrt{\varepsilon}\, d\mathbb{W}, \tag{4}$$

where

$$\mathbb{C} = \exp(-\tau\mathbb{A}^{\mathrm{T}})\exp(-\tau\mathbb{A}), \tag{5}$$

approximates the Cauchy-Green tensor with τ representing a short *decorrelation time*. As shown by Eq. (4), the RFD model has two timescale parameters. They are the decorrelation time τ, which is assumed to be the Kolmogorov timescale τ_K, and T identifying with the *integral timescale*. Therefore, on dimensional grounds, the role of Reynolds number is played by the parameter $r = (\tau/T)^{-2}$. We remark that while this parameter *scales* like a Reynolds number, it is not identical in value to the Reynolds-number in actual fluid flow. For example, Ref. [45] compares the RFD at $\tau/T = 0.1$ against DNS at $Re_\lambda \approx 150$, showing for example comparable intermittency trends. Additionally, increasing r in the RFD above a threshold (around 400) leads to unphysical results and eventually to a numerical blow up [26,29,45].

To reach a statistical equilibrium, a tensorial stochastic force $\mathbb{W}(t)$ has been introduced into Eq. (4). Its strength is determined by a parameter ε, which we pick as $\varepsilon = 0.25$. The force is correlated as

$$\mathbb{E}[dW_{ij}(t)dW_{kl}(t)] = G_{ijkl}\,dt, \tag{6}$$

where the fourth-order tensor,

$$G_{ijkl} = 2\delta_{ik}\delta_{jl} - \tfrac{1}{2}\delta_{il}\delta_{jk} - \tfrac{1}{2}\delta_{ij}\delta_{kl}, \tag{7}$$

is consistent with both the isotropy assumption and incompressibility.

As a small-scale quantity, $\mathbb{A}$ is expected to scale with $1/\tau$. Indeed, the phenomenology of turbulence states that

$\langle \mathrm{Tr}(S^2)\rangle = 1/(2\tau_K^2)$, suggesting a nondimensionalization of the RFD equation with τ. In this setting, the modeled Cauchy-Green tensor would depend weakly on the Reynolds number since the explicit τ-dependence would be absent. When nondimensionalizing with τ, the deterministic part of the RFD would depend on r only through the viscous term. Conversely, the dimensionless noise amplitude gets smaller as the Reynolds number is increased [28] because it scales with a positive power of the small timescale like τ^3. Here, though, we nondimensionalize with T, according to [26,46,47]. With this choice, τ still appears in the modeled Cauchy-Green tensor as a small parameter. As a consequence, expansion and truncation of the Cauchy-Green tensor can be carried out, which, in turn, simplifies the instanton Eqs. (29) (see also the Appendix). In addition, this truncation allows for a qualitative discussion regarding the emergence of extreme passive scalar gradients in Sec. V. With this in mind, the nondimensionalized RFD takes the form

$$d\bar{\mathbb{A}} = \left(-\bar{\mathbb{A}}^2 + \frac{\mathrm{Tr}(\bar{\mathbb{A}}^2)}{\mathrm{Tr}(\bar{\mathbb{C}}^{-1})}\,\bar{\mathbb{C}}^{-1} - \frac{\mathrm{Tr}(\bar{\mathbb{C}}^{-1})}{3}\,\bar{\mathbb{A}}\right) d\bar{t} + \sqrt{\bar{\varepsilon}}\, d\bar{\mathbb{W}}\,, \tag{8}$$

where the dimensionless variables are defined according to

$$\begin{aligned} &\bar{t} = \frac{t}{T}, \quad \bar{\mathbb{A}} = T\mathbb{A}, \quad \bar{\tau} = \frac{\tau}{T}, \\ &\bar{\mathbb{C}} = \exp(-\bar{\tau}\bar{\mathbb{A}}^{\mathrm{T}})\exp(-\bar{\tau}\bar{\mathbb{A}}), \\ &\bar{\varepsilon} = T^3\varepsilon, \quad \bar{\mathbb{W}} = \sqrt{T}\,\mathbb{W}. \end{aligned} \tag{9}$$

Hereafter, we are taking $r \in \{25, 100, 156, 278\}$. To compare our simulations to real turbulence, we computed the flatness of our MC simulations and found $\langle (A_l - \langle A_l\rangle)^4\rangle / \langle (A_l - \langle A_l\rangle)^2\rangle^2 = 3.52$ for the largest value $r = 278$ (where A_l stands for the longitudinal velocity gradients). According to data in Refs. [48,49] a rough estimate of the maximum Taylor-Reynolds number (Re_λ) attained by RFD simulations is $Re_\lambda \approx 20$. In addition, Ref. [50] reports that the skewness of value 0.4 is compatible with $Re_\lambda \approx 20$. This agrees with the RFD result of skewness $\langle (A_l - \langle A_l\rangle)^3\rangle / \langle (A_l - \langle A_l\rangle)^2\rangle^{3/2} = 0.39$ for $r = 278$. While this is a fairly low Re_λ-regime, it nevertheless leads to fat-tailed distributions for the passive scalar gradients, as depicted in Fig. 4.

B. Passive scalar turbulence in the recent fluid deformation model

In a similar manner, taking the gradient of the PSE (2) yields

$$\frac{d\psi_i}{dt} = -A_{ji}\,\psi_j + \kappa\,\frac{\partial^2\psi_i}{\partial x_j \partial x_j}; \quad \psi = \nabla\theta \in \mathbb{R}^3. \tag{10}$$

Following the same rationale of the previous section, the PS-RFD is derived from closing the diffusive Laplacian with the help of the short-time Cauchy-Green tensor and a *diffusive integral timescale* T_θ, yielding [31],

$$d\psi = \left(-\mathbb{A}^{\mathrm{T}}\,\psi - \frac{\mathrm{Tr}(\mathbb{C}^{-1})}{3T_\theta}\psi\right) dt + \sqrt{\varepsilon}\, dF\,, \tag{11}$$

where F denotes a random force that is white in time with amplitude ε, whose correlation reads $\mathbb{E}[dF_i(t)\,dF_j(t)] = \delta_{ij}\,dt$. Hereafter, we assume that the noise strength is the same in both stochastic Eqs. (4) and (11). Reference [31] investigates the statistical characteristics of the kinematics of the RFD passive gradient, whereas Ref. [32] compares the PDFs from Eq. (11) and the DNS, revealing the presence of heavy tails.

In terms of dimensionless variables Eq. (9), the PS-RFD becomes

$$d\bar{\psi} = \left(-\bar{\mathbb{A}}^{\mathrm{T}}\bar{\psi} - \frac{\mathrm{Tr}(\bar{\mathbb{C}}^{-1})}{3\bar{T}_\theta}\bar{\psi}\right) d\bar{t} + \sqrt{\bar{\varepsilon}}\, d\bar{F}, \tag{12}$$

where $\bar{\psi} = T\psi$, $\bar{F} = \sqrt{T}F$ are introduced as the dimensionless passive scalar gradient and random forcing, respectively, $\bar{T}_\theta = T_\theta/T$ is the dimensionless diffusive constant and $\bar{\mathbb{C}}$ is provided by Eq. (9). It is tempting to identify the dimensionless timescale with the Schmidt Sc number as it measures the ratio ν/κ. However, as pointed out by Ref. [31], $\mathrm{Sc} = \nu/\kappa \approx (T_\theta/T)[(\partial X)^2/(\partial X_\theta)^2]$, where ∂X and ∂X_θ are the smallest scales reached by velocity gradient and scalar gradient, respectively. The assumption made by the model considers $\partial X = \partial X_\theta$, that is, the smallest scales of turbulence are of the same order of the smallest scales of the diffusive process. It is known from the phenomenology of turbulence that these length scales are of the same order only for Sc near unity. As a result, the PS-RFD is limited to Sc close to unity [31]. A Lagrangian model for passive scalar gradients similar to the PS-RFD which accounts for Schmidt number dependence is lacking yet. The role of $\bar{T}_\theta$ and r in the development of extreme events shall be discussed in Sec. V. Subsequently, we will be working with the dimensionless RFD and PS-RFD with the bar suppressed for notational clarity.

Equation (11) was conceived to model isotropic passive scalar fluctuations. Nevertheless, a more standard setup investigated both in experiments [51] and numerical simulations [20,21] is the one in which there is an imposed mean passive scalar gradient. In the presence of this large-scale mean profile, experiments reveal a persistent skewness in the direction of mean gradient regardless of Reynolds numbers [51,52]. This observation indicates a violation of the postulate of local isotropy, usually assumed in the context of Kolmogorov theory [7], where anisotropies introduced by the large scale forcing mechanism vanishes as one approaches the smallest scales of motion for high Reynolds numbers. This anomaly is attributed to the formation of ramp-cliff structures. See Ref. [21] for a recent investigation on the role of these structures in the contribution to odd-order moments statistics.

In light of that, we will adapt the original PS-RFD to include a uniform mean derivative scalar in a given direction. Starting from Eq. (10), supplementing a passive scalar mean gradient corresponds to replacing $\psi \to \psi + \Psi$, with a constant $\Psi \in \mathbb{R}^3$. The diffusive term is unaffected by this change so that no further modeling is required. As a result, the PS-RFD closure subjected to a uniform mean gradient reads

$$d\psi = \left(-\mathbb{A}^{\mathrm{T}}(\psi + \Psi) - \frac{\mathrm{Tr}(\mathbb{C}^{-1})}{3T_\theta}\psi\right) dt + \sqrt{\varepsilon}\, dF\,. \tag{13}$$

Without loss of generality, we are considering $\Psi = (1, 0, 0)$ from now on. After simulating Eq. (13), we observed that the model captures the prevailing skewness along the direction of the mean gradient, which can be seen from the asymmetry of

the pdf (Fig. 4). Though many works report a skewness of order unity [21,49,51], our results point to skewness approximately in the range 3–4.4 with a slight upward trend toward increasing r. These higher values of skewness may indicate that the model emulates a Schmidt number lower than unity since the odd-order moments decrease as Sc increases [21]. For the fifth-order normalized moment, no significant trend was found.

III. REDUCED RFD AND PASSIVE SCALAR RFD MODELS

Conditioning on large strain values in the RFD model, and similarly on large passive scalar gradients in the PS-RFD system reveals a statistical tendency to respect axial and reflective symmetries around the axis prescribed by the dominant strain. This has been observed before for the RFD model [53], and for PS-RFD [54], leading to a simplification of both RFD and PS-RFD models. This motivates us here to discuss some details of this dimensional reduction, in particular, how spontaneous symmetry breaking at large strain values leads to a failure of the symmetry-based reduction.

A. Dimensional reduction of the RFD model

The RFD model Eq. (8) describes the evolution of a 3×3 matrix $\mathbb{A}$, but in fact has only five independent variables: This is easily understood following the standard decomposition of the velocity gradient into symmetric and anti-symmetric parts, namely, $A_{ij} = S_{ij} + \Omega_{ij}$, where $S_{ij} = (A_{ij} + A_{ji})/2$ and $\Omega_{ij} = (A_{ij} - A_{ji})/2$ represent the rate of strain and rate of rotation tensors, respectively. By diagonalizing S_{ij}, only three of the six variables in S_{ij} remain. The interpretation is that after diagonalization, the coordinate system is aligned with the principal axis of strain, from which only two are independent due to $\mathrm{Tr}(\mathbb{A}) = \mathrm{Tr}(S) = 0$. The rotation matrix's three variables represent the rate of rotation with respect to each principal axis. Explicitly,

$$\mathbb{A} = \begin{bmatrix} a & 0 & 0 \\ 0 & b & 0 \\ 0 & 0 & c \end{bmatrix} + \frac{1}{2}\begin{bmatrix} 0 & -\omega_c & \omega_b \\ \omega_c & 0 & -\omega_a \\ -\omega_b & \omega_a & 0 \end{bmatrix}, \tag{14}$$

with a, b and $c = -(a + b)$ are the three rates of strain, and ω_a, ω_b, and ω_c are the projections of the vorticity $\omega_i = \epsilon_{ijk}\Omega_{kj}$ along the principal axes.

Consider the case of conditioning on a large value for the first longitudinal component of the velocity gradient, e.g., $A_{11}(t_f)$ takes a value a. It is clear that

$$A_{11} = [\Lambda(\alpha)\,\mathbb{A}\,\Lambda^{\mathrm{T}}(\alpha)]_{11}, \tag{15}$$

where $\Lambda(\alpha)$ is the rotation matrix with respect to x_1 axis, namely,

$$\Lambda(\alpha) = \begin{bmatrix} 1 & 0 & 0 \\ 0 & \cos\alpha & \sin\alpha \\ 0 & -\sin\alpha & \cos\alpha \end{bmatrix}. \tag{16}$$

Equation (15) simply means that many different configurations of $\mathbb{A}$ lead to the same A_{11}, namely those obtained by rotating about the x_1 axis, which is a manifestation of the axial symmetry. Indeed, by arguments of isotropy, the probability obeys $P(\mathbb{A}) = P[\Lambda(\alpha)\mathbb{A}\Lambda^{\mathrm{T}}(\alpha)]$.

We can, in addition, demand that $\mathbb{A}$ *itself* is axisymmetric. This corresponds to a situation where we assume that only the x_1-component of the strain is relevant, and we are free to ignore the others. In this case, the number of degrees of freedom can be reduced even more. Let an infinitesimal rotation about the x_1 axis given by $\Lambda_{ij} = \delta_{ij} + \alpha\,\epsilon_{1ij} + \mathcal{O}(\alpha^2)$. After this transformation, the velocity gradient reads

$$A'_{ij} = A_{ij} + \alpha\,(\epsilon_{1ik}A_{kj} + \epsilon_{1jl}A_{il}). \tag{17}$$

With the hypothesis that $\mathbb{A}$ is invariant under rotations with respect to x_1, that is, $A'_{ij} = A_{ij}$, it can be shown that $\mathbb{A}$ takes the form

$$\mathbb{A} = \begin{bmatrix} a & 0 & 0 \\ 0 & -a/2 & -\omega_a/2 \\ 0 & \omega_a/2 & -a/2 \end{bmatrix}. \tag{18}$$

As a result, the number of degrees of freedom was reduced from 5 to 2. One of them is related to the rate of strain, a, and the other is related to the vorticity. By invoking the reflection transformation over the x_2-x_3 plane (i.e., $x_1 \to -x_1$) and admitting that $\mathbb{A}$ respects this symmetry as well, we have that $\omega_a = -\omega_a = 0$, and only one degree of freedom remains.

In summary, diagonalizing the rate of strain tensor reduces the degrees of freedom from nine to five. Furthermore, assuming invariance of rotation about one of the principal axis of strain (axial symmetry) implies that the vorticity lines up with the principal axis, so that a single component of the vorticity remains, decreasing the number of independent variables by two. Additionally, the same axial symmetry demands the two rates of strain to be the same, which implies two degrees of freedom left. Finally, the assumption that the velocity gradient respects reflection symmetry requires a zero vorticity; otherwise, the symmetry would be broken. As a result, only a single degree of freedom is left, corresponding to the axial rate of strain.

Based on these arguments, we can devise a simplified stochastic model that accounts for the same statistics of the longitudinal component of the RFD model Eq. (8), which we call *reduced* RFD [53], given by

$$\frac{da}{dt} = v(a) + \sqrt{\varepsilon}\,\eta, \tag{19}$$

where a corresponds to A_{11} and

$$v(a) = -a^2 + \frac{3}{2}a^2\frac{e^{-\frac{2a}{\sqrt{r}}}}{e^{-\frac{2a}{\sqrt{r}}} + 2e^{\frac{a}{\sqrt{r}}}} - \frac{a}{3}\left(e^{-\frac{2a}{\sqrt{r}}} + 2e^{\frac{a}{\sqrt{r}}}\right). \tag{20}$$

The noise term $\eta(t)$ is a zero-mean white scalar random variable.

One may ask whether the assumption of invariance under rotation of $\mathbb{A}$ is always valid. The answer is no. As it will be discussed in Sec. III B, there is a critical r above which the velocity gradient $\mathbb{A}$ fails to share the same symmetry of the probability, and the system undergoes a symmetry breaking, closely related to spontaneous symmetry breaking featuring in other areas of physics [55,56]. Hence, the dimensional reduction is no longer possible. Crucially, this critical r coincides with similar limitations of the original RFD model [26].

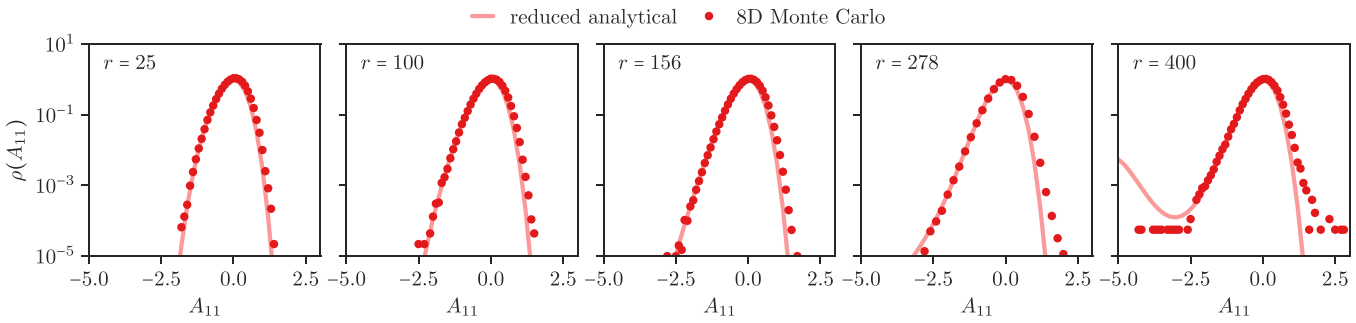

FIG. 1. PDFs of the A_{11} component of the velocity gradient tensor $A_{ij} = \partial u_i/\partial x_j$, for a range of Reynolds numbers. The red dots show a histogram of a MC for the full RFD model Eq. (8), compared against the analytical prediction of the reduced RFD system Eq. (19) (solid line). It shows the emergence of another fixed point of the 1D reduced system at $A_{11} = -3.01$ for $r = 400$, which is an artifact of the model reduction.

B. Numerical results for symmetry breaking of the RFD model

Here we give evidence for the validity of the dimensionally reduced model Eq. (19) for moderate r, and the eventual symmetry breaking of the full 8D model Eq. (8). We recall that for the reduced RFD, an analytical PDF can be easily found by solving the corresponding Fokker-Planck equation [53]. Shown in Fig. 1 are the PDFs obtained via MC simulations (red dots), in the range $r \in [25, 400]$, against the analytical PDFs of the reduced model (solid red lines). For the lowest r values up to $r = 156$, there is a reasonable agreement between the full 8D-RFD and the reduced 1D-RFD. For higher r, a disagreement is seen in the right tail; note, though, that positive strain values are irrelevant for the development of large passive scalar gradients, as will be shown later. As r is increased further to $r = 400$ ($\tau/T = 0.05$), at the very right of Fig. 1, the disagreement becomes more pronounced, including on the far left tail. Here, the 1D-RFD predicts a bimodal PDF with a new local minimum located at $A_{11} = -3.01$. By contrast, this bimodality is not observed in the 8D-RFD. The emergence of this bimodal profile remains for larger values of Reynolds number. Roughly $r = 400$ establishes the upper limit where the dimensional reduction can sensibly be applied.

The discrepancy between 8D-RFD and 1D-RFD demonstrates that for $r \gtrsim 400$ the hypothesis of symmetries (axial and reflection) outlined in the previous section do not hold. Consequently, other components of the velocity gradient start to play a role in the dynamics and may not be neglected. However, it remains true that the equation itself, and thus also the PDF, remains invariant under rotations and reflections for any value of the parameter r. Only individual sample trajectories break the symmetry, while the statistics remain symmetric. Hence, it makes sense to borrow a terminology of condensed matter/high-energy physics [55,56], observing that the model undergoes spontaneous symmetry breaking, since the symmetry of the model is not realized by the individual states of the system $\mathbb{A}$, even though the action and consequently the PDF does observe it. The fact that this indeed happens can be shown numerically. Figure 2 shows the joint PDFs $\rho(\omega_2, \omega_3|A_{11})$ of the perpendicular components of the vorticity $\omega_i = \epsilon_{ijk}\Omega_{kj}$, conditioned on relatively large negative A_{11} at different r. In other words, this shows the distribution of the vorticity vector in the presence of extreme strain, in the plane perpendicular to the strain axis. For moderate $r = 100$ and 400 the distribution is concentrated around 0, highlighting that the vorticity vector points along the strain axis (or is altogether zero). For very large r, though, the perpendicular vorticity components prefer to occupy a ring away from (0,0), indicating the breakdown of axisymmetry for the individual sample. At this r, vorticity is more likely to be at an angle against the strain axis. Note that while we do not believe that the RFD model remains a valid description of 3D NSE turbulence in this regime; we remark that symmetry breaking *has* recently been observed for extreme strain events in full 3D Navier-Stokes [57].

It is worth mentioning that in same range of r where the symmetry breaking happens, the RFD model itself becomes problematic as well, as numerical instabilities start to appear, as reported by Ref. [26]. Here, we shall briefly explain that by considering the high-r limit of Eq. (8). In the limit of infinite r, the RFD model reduces to

$$d\mathbb{A} = \left(-\mathbb{A}^2 + \frac{\mathrm{Tr}(\mathbb{A}^2)}{3}\mathbb{I} - \mathbb{A}\right)dt + \sqrt{\varepsilon}\, d\mathbb{W}\,. \tag{21}$$

Apart from the stochastic forcing, this equation corresponds to the linear damping closure proposed by Ref. [58]. It has been shown that the linear damping is not enough to counteract the strong nonlinearities of the self-stretching and pressure Hessian terms, being subject to finite-time singularities.

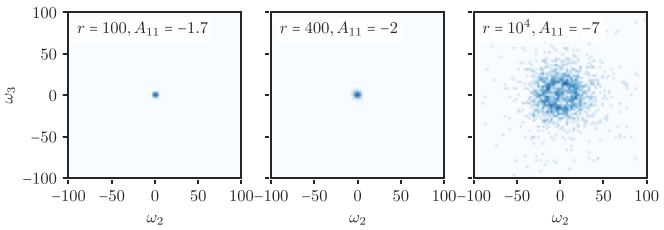

FIG. 2. The joint PDF $\rho(\omega_2, \omega_3|A_{11})$ of the perpendicular components of the vorticity, conditioned on relatively large negative strain values A_{11}, for different values of r. As r increases, the originally very small variances around the most likely configuration $(\omega_2, \omega_3) = (0, 0)$ grows in variance. At high r, a zero perpendicular vorticity is no longer predominant. Instead, the most likely vorticity clusters on a ring, indicating a spontaneous symmetry breaking of the vorticity conditioned on large negative strain.

C. Dimensional reduction of the passive scalar RFD model

Following the same logic, one may derive a two-dimensional reduced model for the PS-RFD by considering the statistics of only a single component of the passive scalar gradient, namely, $\psi_1 = \nabla_1\theta$ which points toward the imposed mean gradient $\Psi = (1, 0, 0)$. More specifically, assuming now that both $\mathbb{A}$ and ψ are invariant under rotation around the x_1 axis, the components ψ_2 and ψ_3 must vanish. As a result, the reduced version of the PS-RFD model Eq. (12) is defined as [54]

$$\frac{d\psi_1}{dt} = b(\psi_1, a) + \sqrt{\varepsilon}\,\xi, \tag{22}$$

where

$$b(\psi_1, a) = -(\psi_1 + 1)\,a - \left(e^{-\frac{2a}{\sqrt{r}}} + 2\,e^{\frac{a}{\sqrt{r}}}\right)\frac{\psi_1}{3\,T_\theta}, \tag{23}$$

and $\xi(t)$ is a white scalar noise that is independent of $\eta(t)$ in Eq. (19). The dynamics of $\psi_1(t)$ depend on the longitudinal velocity gradient $a(t)$. Thus, Eq. (22) has to be solved together with Eq. (19).

Being dependent on the RFD, it is clear that the dimensional reductions for PS-RFD will fail in the same range of r where RFD symmetry breaks down, but is in excellent agreement for $r \lesssim 400$. Next, the instanton equations and their simplified version for the PS-RFD system are obtained. Since there is a significant gain in numerical efficiency in solving the instanton equations of the reduced system, we will do so whenever the dimensional reduction is justified.

IV. INSTANTON FORMALISM AND EXTREME EVENTS

In this section, we apply the instanton formalism to the PS-RFD model described in Sec. II. Intuitively, the instanton formalism relies on the fact that in some limit (such as the small noise or extreme event limits) probabilities can be efficiently estimated through a prototypical "placeholder" event that observes the same scaling as the actual probability. A probability of an event is always a sum (or integral) over all possible ways the event can occur, weighted by its respective probability. In the limit, this integral can be approximated by a saddlepoint approximation or Laplace method, giving the leading order exponential contribution. For example, we are interested in the probability of observing events of extreme passive scalar gradients at the final time, $P[\psi_1(t_f) > z]$. Then, the instanton formalism postulates that the probability scales like an exponential,

$$P(\psi_1(t_f) > z) \sim \exp[-\varepsilon^{-1} I(z)]. \tag{24}$$

The exponential scaling, given by the *rate function* $I(z)$, can be obtained by evaluating an action $S[\mathbb{A}, \psi]$ at the *instanton* $(\mathbb{A}^*, \psi^*)$,

$$I(z) = S[\mathbb{A}^*, \psi^*] = \inf_{\psi_1(t_f)>z} S[\mathbb{A}, \psi], \tag{25}$$

where the instanton is the minimizer of the action. We will derive the action for the PS-RFD model in Sec. IV B. In our setup, the instanton formalism is equivalent to sample path large deviation theory [36,37,59].

A. Related works

The action functional for the RFD model has first been determined in Ref. [47]. The instanton equations were linearized in this reference to derive an approximate analytical solution, with additional consideration of the fluctuations around the linearized instanton. As a result, to leading order in the perturbative expansion, the fluctuations yield an effective action with renormalized noise. That is, to first order, the fluctuations around the instanton can be taken into account by renormalizing the noise correlator. This approach was used to evaluate the PDFs of the velocity gradient and the joint PDF of the R and Q invariants.

By contrast, Ref. [53] determines the instanton numerically by solving the corresponding highly nonlinear RFD Hamilton's equations with the *Chernykh-Stepanov* (C-S) algorithm [60]. Further, following the perturbation techniques outlined in Ref. [47], a detailed analytical treatment of the RFD closure has been given by Ref. [61], providing a hierarchical classification of several Feynman diagrams. In addition to the noise renormalization, Ref. [61] also computes the propagator renormalization derived from a linear instanton approximation. The resulting PDFs are compared with the ones from Ref. [53] with good agreement.

More recently, Ref. [54] applies instanton arguments also to the PS-RFD model, proposing a parametric form of the Hamilton's equation. Aside from that, a perturbation expansion has been carried out along the lines of Refs. [47,61] to account for instanton path fluctuations.

Putting these results into perspective, all are capable of obtaining only mild non-Gaussian PDFs, that is, they work for a restricted range of τ, namely, $\tau/T \geqslant 0.1$ ($r \lesssim 100$). As r increases, and intermittency starts to play a role, the probability distributions develop heavy tails. Consequently, the corresponding rate function ceases to be convex, which prevents naive instanton approaches based on the Gärtner-Ellis theorem to remain well-posed. To overcome this and to apply the instanton formalism to more turbulent flows, here we introduce a nonlinear convexification to treat the heavy-tailed distribution, as discussed in Sec. V.

B. The action and instanton equations for the PS-RFD dynamics

In accordance with [54], the PS-RFD action reads [62–64],

$$S[\mathbb{P}, \mathbb{A}, \Pi, \psi] = \int_{t_i}^{t_f} dt \Big(\mathrm{Tr}\{\mathbb{P}^{\mathrm{T}}[\dot{\mathbb{A}} - \mathbb{V}(\mathbb{A})]\} - \frac{1}{2}P_{ij}G_{ijkl}P_{kl} + \Pi^{\mathrm{T}}[\dot{\psi} - M(\psi, \mathbb{A})] - \frac{1}{2}\Pi^{\mathrm{T}}\Pi\Big), \tag{26}$$

where

$$M(\psi, \mathbb{A}) = -\mathbb{A}^{\mathrm{T}}(\psi + \Psi) - \frac{\mathrm{Tr}(\mathbb{C}^{-1})}{3T_\theta}\psi, \tag{27}$$

and

$$\mathbb{V}(\mathbb{A}) = -\mathbb{A}^2 + \frac{\mathrm{Tr}(\mathbb{A}^2)}{\mathrm{Tr}(\mathbb{C}^{-1})}\,\mathbb{C}^{-1} - \frac{\mathrm{Tr}(\mathbb{C}^{-1})}{3}\mathbb{A}, \tag{28}$$

stand for the drift terms of Eqs. (12) and (8), respectively, and $\Pi \in \mathbb{R}^3$ ($\mathbb{P} \in \mathbb{R}^{3\times3}$) is the conjugated momentum of ψ ($\mathbb{A}$),

closely related to the auxiliary variables of the Martin-Siggia-Rose-Janssen-de Dominicis formalism [62–64].

The minimum of the action functional Eq. (26) is achieved by the solutions of the following corresponding instanton equations of the fields $\mathbb{A}$, ψ:

$$\begin{aligned}
&\frac{\delta S}{\delta P_{ij}} = 0, \Rightarrow \dot{A}_{ij} = V(\mathbb{A})_{ij} + G_{ijkl}\, P_{kl},\\
&\frac{\delta S}{\delta A_{ij}} = 0, \Rightarrow \dot{P}_{ij} = -P_{kl}\, \nabla_{A_{ij}} V(\mathbb{A})_{kl} - \Pi_k\, \nabla_{A_{ij}} M(\psi, \mathbb{A})_k,\\
&\frac{\delta S}{\delta \Pi_k} = 0, \Rightarrow \dot{\psi}_k = M(\psi, \mathbb{A})_k + \Pi_k,\\
&\frac{\delta S}{\delta \psi_k} = 0, \Rightarrow \dot{\Pi}_k = -\Pi_n\, \nabla_{\psi_k} M(\psi, \mathbb{A})_n,
\end{aligned} \tag{29}$$

for $t \in [t_i, t_f]$. The full formulas for these gradients are derived in the Appendix, where we expand the drifts up to second order [47].

These four coupled Eqs. (29) are solved simultaneously using the C-S scheme [60,65], which corresponds effectively to a gradient descent of the constrained optimization problem [66]. The boundary conditions of Eqs. (29) are specified by the choice of observable. Here, we are looking for events where one component ψ_j of the passive scalar gradient exceeds a threshold z, which leads to

$$\mathbb{A}(t_i) = \mathbf{0}, \quad \psi(t_i) = 0, \quad \mathbb{P}(t_f) = \mathbf{0}, \quad \Pi_j(t_f) = \lambda\, \nabla F[\psi_j(t_f)], \tag{30}$$

where the initial values of the fields are their stable equilibrium points, the origin. The final time constraint on the gradient of passive scalar to attain $z = \psi_j(t_f)$ is implemented in Eq. (30) through a Lagrange multiplier $\lambda \in \mathbb{R}$, [67]. The function $F : \mathbb{R} \to \mathbb{R}$ is a nonlinear reparametrization to ensure there is a unique λ for every large passive scalar gradients of interest [44].

C. Instantons for the reduced PS-RFD dynamics

The full instanton Eqs. (29) correspond to the system Eqs. (8) and (12). However, when a final time constraint is imposed on a component of the passive scalar, such as $F[\psi_1(t_f)]$ Eq. (30), it exhibits symmetric behavior (with respect to axial and reflective symmetries) that reduce this 11-variable system to one with only two leading variables, $\psi_1(t)$ and $a(t)$. The same reduction applies to conditioning on other components of ψ. As discussed in Sec. III, this reduction is valid for $r \lesssim 400$.

For the reduced model Eqs. (19) and (22), the resulting 2D instanton equations are

$$\begin{aligned}
\dot{a} &= v(a) + p,\\
\dot{p} &= -p\, \frac{\partial v(a)}{\partial a} - q\, \frac{\partial b(\psi_1, a)}{\partial a},\\
\dot{\psi}_1 &= b(\psi_1, a) + q,\\
\dot{q} &= -q\, \frac{\partial b(\psi_1, a)}{\partial \psi_1},
\end{aligned} \tag{31}$$

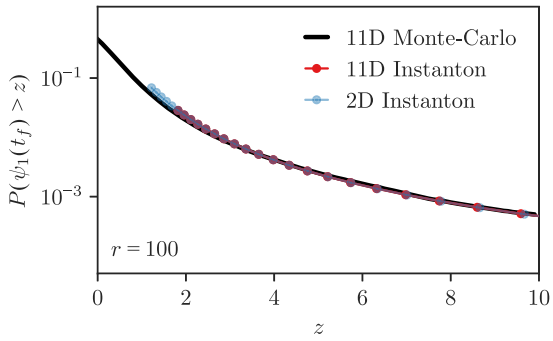

FIG. 3. The complementary cumulative distribution functions of passive scalar gradients $P(\psi_1(t_f) > z)$, (solid line) compared to the outcomes of both 11D and 2D instantons results (red and blue, respectively), with $r = 100$ and $T_\theta = 1$. Both the full and the reduced instantons agree with MC simulations of the full system.

where $p(t) = P_{11}(t)$ and $q(t) = \Pi_1(t)$. The drifts $v(a)$ and $b(\psi_1, a)$ are derived in the reduced models' Sec. III, namely, Eqs. (20) and (23).

The difference between Eqs. (29) and (31) is that the latter is more computationally efficient than the former due to the significant reduction of its dimensions, and we will use it in the following to estimate the tail probabilities of the passive scalar gradient. Figure 3 demonstrates numerically that this simplification is indeed justified for the instanton, as the predicted probabilities $P[\psi_1(t_f) > z]$ of exceeding a passive scalar gradient z at final time t_f is in excellent agreement between MC sampling of the full RFD model, and the instanton estimates of both the full and the reduced models.

V. EXTREME GRADIENT OF THE PASSIVE SCALAR

In this section we provide both analytical and numerical results for extreme passive scalar gradients in the PS-RFD. Starting from the model Eqs. (12), which we rewrite here for convenience,

$$\begin{aligned}
d\psi &= \left(-\mathbb{A}^{\mathrm{T}}(\psi + \Psi) - \frac{\mathrm{Tr}(\mathbb{C}^{-1})}{3T_\theta}\psi\right) dt + \sqrt{\varepsilon}\, dF\,;\\
\mathbb{C} &= e^{\frac{\mathbb{A}}{\sqrt{r}}} e^{\frac{\mathbb{A}^{\mathrm{T}}}{\sqrt{r}}},
\end{aligned} \tag{32}$$

recall that the first term on the right-hand side (RHS) of this stochastic equation accounts for the advection, whereas the second term describes the effect of diffusion. We shall discuss the role played by parameters T_θ and r. In the limit of high r, the Cauchy-Green tensor $\mathbb{C}$ can be expanded to order $\mathcal{O}(r^{-1})$,

$$\begin{aligned}
\mathrm{Tr}(\mathbb{C}^{-1}) &= 3 + \frac{1}{2r}\mathrm{Tr}(\mathbb{A}^2 + \mathbb{A}^{2\mathrm{T}} + 2\mathbb{A}^{\mathrm{T}}\mathbb{A})\\
&= 3 + \frac{2}{r}\mathrm{Tr}(S^2),
\end{aligned} \tag{33}$$

where S is the rate of strain tensor $S = (\mathbb{A} + \mathbb{A}^{\mathrm{T}})/2$. Taking this into consideration, Eq. (32) is rewritten as

$$d\psi = \left(-\mathbb{A}^{\mathrm{T}}(\psi + \Psi) - \frac{\psi}{T_\theta} - \frac{2\psi}{3T_\theta\, r}\mathrm{Tr}(S^2)\right) dt + \sqrt{\varepsilon}\, dF\,. \tag{34}$$

From Eq. (34), it is clear that the second term on the right side is linear damping for ψ, acting to decrease the size of fluctuations, with T_θ being the (dimensionless) characteristic time. The behavior of the third term, however, can be understood as follows: Finiteness of dissipation [recall the scaling we use (8)] reads $\langle \mathrm{Tr}(S^2)\rangle = r/2$. As a result, the third term is expected to remain bounded, on average, as r increases. By contrast, the first term is expected to get larger (in absolute value) since $\mathbb{A}$, on phenomenological grounds, is expected to scale as $\mathbb{A} \approx T/\tau$. Hence, as r increases keeping T_θ constant, the effect of the advection (first term) overcomes the third term that accounts for modeled turbulent-diffusion effects.

Our claim is that as the parameters T_θ or r are increased, the development of a large passive scalar gradient can be enhanced. Increasing T_θ leads to lower damping effects played by the second and third terms on the RHS of Eq. (34). Likewise, increasing r enables the advection term to surpass the effect of the third term on the RHS of (34). The advection term, in turn, will contribute to an increase of ψ as long as an eigenvalue of $\mathbb{A}$ associated with the direction of ψ is negative, which means that the compressional directions of the velocity gradient lead to extreme values of the passive scalar gradients. This qualitative analysis meets the known trends in the alignment of the scalar gradient with strain [68,69].

A. Heavy tails and convexification

We are now equipped to investigate the probability to observe extreme passive scalar gradients for different r and T_θ. Figure 4 displays the PDFs of the first component of passive scalar gradients, ψ_1, at the final time t_f, for various values of r in Fig. 4(a), and diffusive timescales T_θ in Fig. 4(b). They are obtained by MC simulations of the full 11D PS-RFD system Eqs. (8) and (12). It illustrates that indeed increasing both r and T_θ invokes heavy tails for the passive scalar gradient due to strong turbulent mixing and high transport rates. We also remark that the fattening of the tails is more sensitive to the diffusive timescale T_θ than to the Reynolds number. This can be understood through Eq. (34), where it is evident that increasing T_θ leads to a decrease of two suppression terms for ψ, compared to only one for r.

B. Extreme configurations of the passive scalar gradient

The probabilities obtained from MC sampling can be directly compared to predictions from the instanton formalism, obtained by solving the optimization problem Eq. (25). In practice, we do so by numerically solving the instanton Eqs. (31). This comes of a significant performance benefit over computing the instanton for the full model Eq. (29), allowing us to compute the minimizer faster. For example, the average speed-up factor for $r = 100$ and $z \in [2, 10]$ is 54. The benefit of solving Eqs. (31) is even more significant for extreme events since this factor of improvement grows as r and/or z increase. To overcome the problem of heavy tails, we convexify the rate function with a reparametrization of the observable according to the scheme presented in Ref. [44]. Concretely, we choose $F(z) = \mathrm{sign}(z) \log\log|z|$, to be inserted as boundary condition into Eq. (30). We then use the C-S algorithm [60,65] to obtain the instanton fields $\mathbb{A}$ and

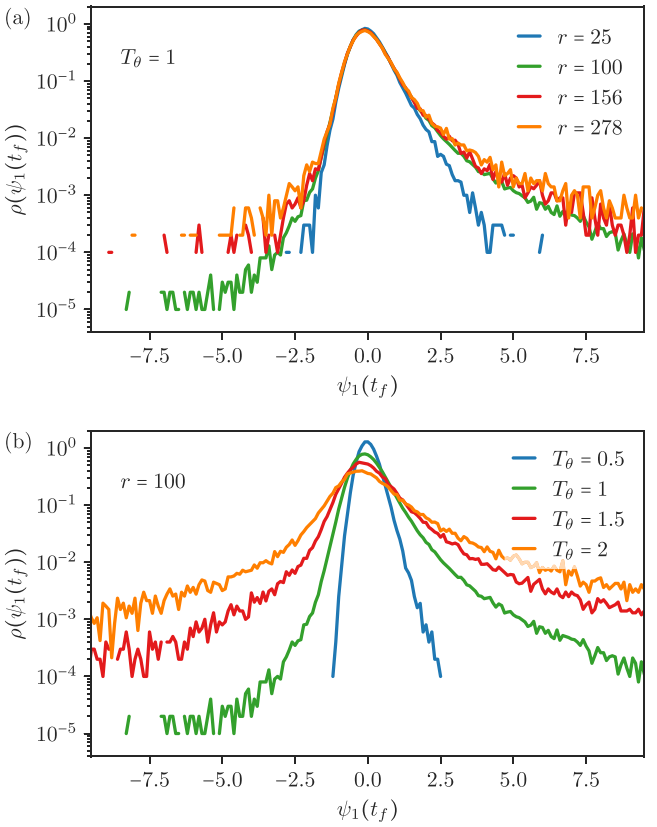

FIG. 4. PDFs of the first component of passive scalar gradients, ψ_1, obtained from MC simulations of the PS-RFD system Eqs. (8) and (12) for various Reynolds numbers r and diffusive timescales T_θ. Subfigure (a) exhibits heavier tails as r increases, where T_θ is set to unity, indicating significant turbulent mixing. Subfigure (b) shows that increasing T_θ at a moderate value of Reynolds number, $r = 100$, results in heavy-tailed gradient distributions, caused by a high transport rate.

ψ and their respective conjugate momenta $\mathbb{P}$ and Π. These allow us to (i) obtain the tail scaling of the passive scalar gradient PDF by computing the action of the instanton, and (ii) identify the mechanism responsible for the formation of extreme passive scalar gradient events within the model.

Figure 5 presents the logarithmic probabilities of MC simulations of the passive scalar $\psi_1(t_f)$ (dotted lines) against 2D instantons results (solid lines) for different values of r, where T_θ is set to unity. It demonstrates an excellent agreement of the tail scaling between the 11D MC simulation and the instanton prediction, in particular, when ψ_1 becomes large. Note that the instanton computation allows us to go extremely far into the tails, where MC becomes inefficient. Figure 6 depicts a set of realizations achieving an extreme passive scalar gradient, $\psi_1 = 6.91$, in the a-ψ_1 plane. Here, the shading indicates the MC density of trajectories that exhibit this large passive scalar gradient at the final time, with samples number equals 367 (filtered out of 3×10^6 trajectories). While the solid line shows the instanton prediction for comparison. Visible is the dominant mechanism for producing large passive scalar gradients: Fluctuations in the relevant strain component drives the system into a region of large negative strain, which deterministically amplifies the passive scalar gradient to large values.

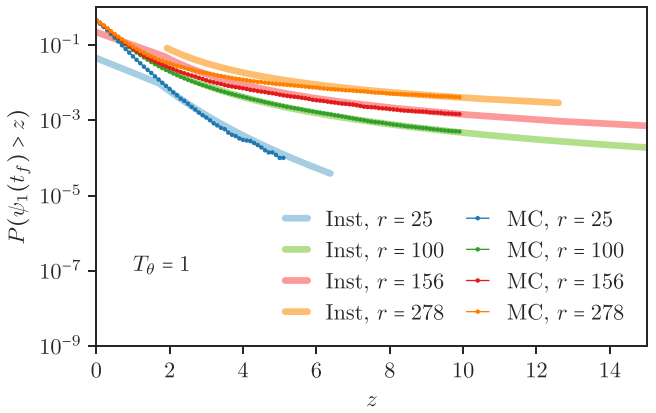

FIG. 5. The complementary cumulative distribution functions of the passive scalar, $P(\psi_1(t_f) > z)$. Compared are MC simulations (dotted lines) against 2D instantons estimates (solid lines) for different values of r (T_θ is set to unity). There is clear agreement between 11D MC and the 2D instanton estimate in particular when ψ_1 becomes large (far tails), in accordance with large deviations theory.

Note that the dominant reactive channel is nicely predicted by the instanton.

VI. CONCLUSION

We investigate events of extreme passive scalar gradients in turbulent flows by using Lagrangian turbulence models extended to handle passive scalar advection. We demonstrate how a reduced two-dimensional model (one component of strain and passive scalar gradient each) captures the important mechanisms responsible for large passive scalar gradients. Notably, the symmetries necessary to apply the reduced model become broken for very extreme events or very large Reynolds numbers, which we can observe by direct sampling. We remark that the full RFD model also fails to describe fully developed Navier-Stokes turbulence in this regime, so that the reduced model remains a helpful simplification for our purposes.

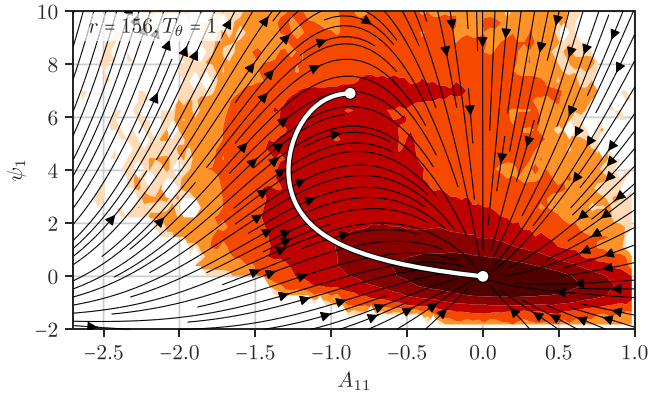

FIG. 6. Events of extreme passive scalar gradient for the reduced model in the a-ψ_1 plane. The streamlines depict the deterministic drift of the reduced PS-RFD model. The line shows the instanton for realizing a final-time event of $\psi(t_f) = 6.91$, starting from the fixed point (0,0) (white line). The density of trajectories of MC-simulations, conditioned on the same outcome, is shown as a heatmap where the samples number equals 367 (filtered out of 3×10^6 trajectories). Extreme outcomes of ψ_1 are commonly achieved by first transitioning into a region of negative strain, in which it is much easier to excite strong gradients. The instanton correctly predicts this mechanism.

We employ the instanton formalism to capture the scaling of very large outlier events in the tails of the PDF of passive scalar gradients. This most likely trajectory not only yields the correct tail scaling, even in the fat-tailed regime, but further allows us to investigate the mechanism responsible for the buildup of large gradients in the reduced model.

ACKNOWLEDGMENTS

The authors thank the anonymous referee for suggesting relevant literature and recommending including the mean background gradient in the passive scalar model. M.A. acknowledges the Ph.D. funding received from UKSACB. T.G. acknowledges the support received from the EPSRC Projects No. EP/T011866/1 and No. EP/V013319/1.

APPENDIX

1. The detailed derivations of the gradients of the drifts

To compute the gradient of the exponential terms of $V(\mathbb{A})$ and $M(\psi, \mathbb{A})$ with respect tensor $\mathbb{A}$, they need to be extended. Up to the second order of τ, the power series of the matrix exponential $e^{\mathbf{X}} = \sum_{n=0}^{\infty} \frac{\mathbf{X}^n}{n!}$ is used for the stationary Cauchy-Green tensor $\mathbb{C}^{-1}$. Notice that it still possesses the physical features of the full drifts of this model [47]. The expansion process is ordered in the following points:

(1) The power series of the matrix exponential to extend $\mathbb{C}^{-1}$ gives

$$\begin{aligned}\mathbb{C}^{-1} &= (e^{\tau\mathbb{A}}\ e^{\tau\mathbb{A}^{\mathrm{T}}})^{-1} \\ &= \left[\sum_{n=0}^{\infty}\frac{(-\tau\mathbb{A}^{\mathrm{T}})^n}{n!}\right]\left[\sum_{n=0}^{\infty}\frac{(-\tau\mathbb{A})^n}{n!}\right] \\ &= \mathbb{I} - \tau(\mathbb{A}+\mathbb{A}^{\mathrm{T}}) + \frac{\tau^2}{2}[\mathbb{A}^2 + 2\,\mathbb{A}^{\mathrm{T}}\mathbb{A} + (\mathbb{A}^{\mathrm{T}})^2] + O(\tau^3).\end{aligned}$$

Then, the trace of $\mathbb{C}^{-1}$ after the truncation to the second order is

$$\mathrm{Tr}(\mathbb{C}^{-1}) = 3 + \tau^2\,\mathrm{Tr}(\mathbb{A}^2) + \tau^2\mathrm{Tr}(\mathbb{A}^{\mathrm{T}}\mathbb{A}), \tag{A1}$$

where the linearity property of the trace operator and the fact that $\mathrm{Tr}(\mathbb{A}) = \mathrm{Tr}(\mathbb{A}^{\mathrm{T}}) = 0$ (due to the incompressibility of the flow) and $\mathrm{Tr}(\mathbb{A}^2) = \mathrm{Tr}[(\mathbb{A}^{\mathrm{T}})^2]$ are used.

(2) Substituting the expanded version of $\mathbb{C}^{-1}$ and its trace in the drift term Eq. (28) gives

$$\begin{aligned}V(\mathbb{A}) = &-\mathbb{A}^2 + \frac{\mathrm{Tr}(\mathbb{A}^2)}{3 + \tau^2\,\mathrm{Tr}(\mathbb{A}^2) + \tau^2\,\mathrm{Tr}(\mathbb{A}^{\mathrm{T}}\mathbb{A})} \\ &\times\left\{\mathbb{I} - \tau\,(\mathbb{A}+\mathbb{A}^{\mathrm{T}}) + \frac{\tau^2}{2}[\mathbb{A}^2 + 2\,\mathbb{A}^{\mathrm{T}}\mathbb{A} + (\mathbb{A}^{\mathrm{T}})^2]\right\} \\ &- \frac{\mathbb{A}}{3}[3 + \tau^2\,\mathrm{Tr}(\mathbb{A}^2) + \tau^2\,\mathrm{Tr}(\mathbb{A}^{\mathrm{T}}\mathbb{A})].\end{aligned} \tag{A2}$$

The quantity $1/[3+\tau^2\,\mathrm{Tr}(\mathbb{A}^2)+\tau^2\,\mathrm{Tr}(\mathbb{A}^{\mathrm{T}}\mathbb{A})]$ can be rewritten in terms of Maclaurin series as follows:

$$\frac{1}{3(1-x)}=\frac{1}{3}\sum_{n=0}^{\infty}x^n,\quad x:=-\frac{1}{3}[\tau^2\,\mathrm{Tr}(\mathbb{A}^2)+\tau^2\,\mathrm{Tr}(\mathbb{A}^{\mathrm{T}}\mathbb{A})].$$

Thus,

$$\frac{1}{3+\tau^2\,\mathrm{Tr}(\mathbb{A}^2)+\tau^2\,\mathrm{Tr}(\mathbb{A}^{\mathrm{T}}\mathbb{A})}=\frac{1}{3}-\frac{1}{9}[\tau^2\,\mathrm{Tr}(\mathbb{A}^2)+\tau^2\,\mathrm{Tr}(\mathbb{A}^{\mathrm{T}}\mathbb{A})]+O(\tau^3).$$

(3) Inserting the last equality into Eq. (A2) and considering only the second-order terms of τ yields the truncation formula of $V(\mathbb{A})$ Eq. (28) [53]:

$$V(\mathbb{A})=\sum_{p=1}^{4}V_p(\mathbb{A}),\tag{A3}$$

where $V_p(\mathbb{A})$ contains all the components of $O(\mathbb{A}^p)$, that is

$$V_1(\mathbb{A})=-\mathbb{A},$$

$$V_2(\mathbb{A})=-\mathbb{A}^2+\frac{\mathbb{I}}{3}\mathrm{Tr}(\mathbb{A}^2),$$

$$V_3(\mathbb{A})=-\frac{\tau}{3}\,\mathrm{Tr}(\mathbb{A}^2)(\mathbb{A}+\mathbb{A}^{\mathrm{T}})-\frac{\tau^2}{3}\,\mathbb{A}\,[\,\mathrm{Tr}(\mathbb{A}^2)+\,\mathrm{Tr}(\mathbb{A}^{\mathrm{T}}\mathbb{A})],$$

$$V_4(\mathbb{A})=-\frac{\tau^2}{9}\,\mathrm{Tr}(\mathbb{A}^2)\,\mathbb{I}\,[\mathrm{Tr}(\mathbb{A}^2)+\mathrm{Tr}(\mathbb{A}^{\mathrm{T}}\mathbb{A})]+\frac{\tau^2}{6}\,\mathrm{Tr}(\mathbb{A}^2)[\mathbb{A}^2+2\,\mathbb{A}^{\mathrm{T}}\,\mathbb{A}+(\mathbb{A}^{\mathrm{T}})^2].$$

(4) Similarly, the extension version of $M(\psi,\mathbb{A})$, resulting from substituting the truncated trace Eq. (A1) into the drift of the PS-RFD Eq. (27), is

$$M(\psi,\mathbb{A})=-\mathbb{A}^{\mathrm{T}}(\psi+\Psi)-\frac{1}{3\,T_\theta}\times[3+\tau^2\,\mathrm{Tr}(\mathbb{A}^2)+\tau^2\,\mathrm{Tr}(\mathbb{A}^{\mathrm{T}}\mathbb{A})]\,\psi.\tag{A4}$$

Now, obtaining the gradient tensors $\nabla_{A_{ij}}V(\mathbb{A})_{kl}$, $\nabla_{A_{ij}}M(\psi,\mathbb{A})_k$ and $\nabla_{\psi_k}M(\psi,\mathbb{A})_n$ [required for instanton Eqs. (29)] from the truncated drifts Eqs. (A3) and (A4) is straightforward computations, as shown:

(1) The first gradient tensor is

$$[\nabla_{\mathbb{A}}V(\mathbb{A})]_{klij}=\nabla_{A_{ij}}V(\mathbb{A})_{kl}=\sum_{p=1}^{4}\nabla_{A_{ij}}V_p(\mathbb{A})_{kl},\tag{A5}$$

where

$$\nabla_{A_{ij}}V_1(\mathbb{A})_{kl}=-\frac{\partial A_{kl}}{\partial A_{ij}}=-\delta_{ki}\delta_{lj},$$

$$\nabla_{A_{ij}}V_2(\mathbb{A})_{kl}=\frac{\partial}{\partial A_{ij}}\left[-A_{kl}^2+\frac{1}{3}\,\delta_{kl}\,\mathrm{Tr}(\mathbb{A}^2)\right]=-\delta_{ki}\,A_{jl}-A_{ki}\,\delta_{lj}+\frac{2}{3}\,\delta_{kl}\,A_{ji},$$

$$\nabla_{A_{ij}}V_3(\mathbb{A})_{kl}=-\frac{\tau}{3}\frac{\partial}{\partial A_{ij}}\{\mathrm{Tr}(\mathbb{A}^2)(A_{kl}+A_{lk})+\tau\,A_{kl}\big[\mathrm{Tr}(\mathbb{A}^2)+\mathrm{Tr}(\mathbb{A}^{\mathrm{T}}\mathbb{A})\,\big]\}$$

$$=-\frac{\tau}{3}\big[2\,A_{ji}(A_{kl}+A_{lk})+\mathrm{Tr}(\mathbb{A}^2)\,(\delta_{ki}\,\delta_{lj}+\delta_{li}\,\delta_{kj})\big]-\frac{\tau^2}{3}\big\{\delta_{ki}\,\delta_{lj}\big[\mathrm{Tr}(\mathbb{A}^2)+\mathrm{Tr}(\mathbb{A}^{\mathrm{T}}\mathbb{A})\,\big]+2A_{kl}(A_{ji}+A_{ij})\big\},$$

$$\nabla_{A_{ij}}V_4(\mathbb{A})_{kl}=\frac{\partial}{\partial A_{ij}}\left\{-\frac{\tau^2}{9}\,\mathrm{Tr}(\mathbb{A}^2)\,\delta_{kl}\,\big[\mathrm{Tr}(\mathbb{A}^2)+\mathrm{Tr}(\mathbb{A}^{\mathrm{T}}\,\mathbb{A})\big]+\frac{\tau^2}{6}\,\mathrm{Tr}(\mathbb{A}^2)\,\big(A_{kl}^2+2\,A_{mk}\,A_{ml}+A_{lk}^2\big)\right\}$$

$$=-\frac{2}{9}\,\tau^2\,\delta_{kl}\,\{A_{ji}\,[2\,\mathrm{Tr}(\mathbb{A}^2)+\mathrm{Tr}(\mathbb{A}^{\mathrm{T}}\mathbb{A})]+\mathrm{Tr}(\mathbb{A}^2)\,A_{ij}\}+\frac{\tau^2}{3}\left\{A_{ji}\,\big(A_{kl}^2+2A_{mk}\,A_{ml}\,+A_{lk}^2\big)+\mathrm{Tr}(\mathbb{A}^2)\right.$$

$$\left.\times\left[\,\delta_{kj}\,A_{il}\,+A_{ik}\,\delta_{lj}+\frac{1}{2}(\delta_{ki}\,A_{jl}+A_{ki}\,\delta_{lj}+\delta_{li}\,A_{jk}+A_{li}\,\delta_{kj})\right]\right\}.$$

The following relations are used:

$$\frac{\partial A_{kl}^2}{\partial A_{ij}}=\delta_{ki}\,A_{jl}+A_{ki}\,\delta_{lj},\quad\frac{\partial\,\mathrm{Tr}(\mathbb{A}^2)}{\partial A_{ij}}=A_{ji}+A_{ji}=2A_{ji},\quad\frac{\partial\,\mathrm{Tr}(\mathbb{A}^{\mathrm{T}}\mathbb{A})}{\partial A_{ij}}=2A_{ij}.$$

(2) The second gradient tensor is

$$[\nabla_{\mathbb{A}}M(\psi,\mathbb{A})]_{kij}=\nabla_{A_{ij}}M(\psi,\mathbb{A})_k=\frac{\partial}{\partial A_{ij}}\left\{-A_{mk}\,(\psi_m+\Psi_m)-\frac{1}{3\,T_\theta}[3+\tau^2\,\mathrm{Tr}(\mathbb{A}^2)+\tau^2\,\mathrm{Tr}(\mathbb{A}^{\mathrm{T}}\mathbb{A})]\psi_k\right\}$$

$$=-\delta_{kj}(\psi_i+\Psi_i)-\frac{2\,\tau^2}{3\,T_\theta}(A_{ji}+A_{ij})\,\psi_k.\tag{A6}$$

(3) The third gradient tensor is

$$[\nabla_\psi M(\psi, \mathbb{A})]_{nk} = \nabla_{\psi_k} M(\psi, \mathbb{A})_n = \frac{\partial}{\partial \psi_k}\left\{-A_{mn}\,\psi_m - \frac{1}{3\,T_\theta}[3 + \tau^2\,\mathrm{Tr}(\mathbb{A}^2) + \tau^2\,\mathrm{Tr}(\mathbb{A}^{\mathrm{T}}\mathbb{A})]\;\psi_k\right\}$$
$$= -A_{kn} - \frac{1}{3\,T_\theta}[3 + \tau^2\,\mathrm{Tr}(\mathbb{A}^2) + \tau^2\,\mathrm{Tr}(\mathbb{A}^{\mathrm{T}}\mathbb{A})]\;\delta_{nk}. \tag{A7}$$

[1] B. I. Shraiman and E. D. Siggia, Nature (London) **405**, 639 (2000).
[2] G. Falkovich, K. Gawedzki, and M. Vergassola, Rev. Mod. Phys. **73**, 913 (2001).
[3] I. Mazzitelli and A. S. Lanotte, Physica D **241**, 251 (2012).
[4] C. Nironi, P. Salizzoni, M. Marro, P. Mejean, N. Grosjean, and L. Soulhac, Boundary-Layer Meteorol. **156**, 415 (2015).
[5] Y. Huang and L. Wang, Phys. Scr. **94**, 014009 (2019).
[6] N. Bhamidipati, A. N. Souza, and G. R. Flierl, Ocean Model. **149**, 101615 (2020).
[7] U. Frisch, *Turbulence* (Cambridge University Press, Cambridge, UK, 1995).
[8] P. Vieillefosse, J. Physique **43**, 837 (1982).
[9] B. J. Cantwell, Phys. Fluids **4**, 782 (1992).
[10] C. Meneveau, Annu. Rev. Fluid Mech. **43**, 219 (2011).
[11] B. W. Zeff, D. D. Lanterman, R. McAllister, R. Roy, E. J. Kostelich, and D. P. Lathrop, Nature (London) **421**, 146 (2003).
[12] J. M. Wallace, Phys. Fluids **21**, 021301 (2009).
[13] D. Buaria, A. Pumir, E. Bodenschatz, and P.-K. Yeung, New J. Phys. **21**, 043004 (2019).
[14] K. D. Squires and J. K. Eaton, Phys. Fluids **3**, 1169 (1991).
[15] E. Balkovsky, G. Falkovich, and A. Fouxon, Phys. Rev. Lett. **86**, 2790 (2001).
[16] R. A. Shaw, Annu. Rev. Fluid Mech. **35**, 183 (2003).
[17] R. H. Kraichnan, Phys. Fluids **11**, 945 (1968).
[18] R. H. Kraichnan, Phys. Rev. Lett. **72**, 1016 (1994).
[19] T. Yasuda, T. Gotoh, T. Watanabe, and I. Saito, J. Fluid Mech. **898**, A4 (2020).
[20] D. Buaria, M. P. Clay, K. R. Sreenivasan, and P. K. Yeung, Phys. Rev. Lett. **126**, 074501 (2021).
[21] D. Buaria, M. P. Clay, K. R. Sreenivasan, and P. K. Yeung, Phys. Rev. Lett. **126**, 034504 (2021).
[22] M. B. Bertagni, M. Marro, P. Salizzoni, and C. Camporeale, Phys. Rev. Fluids **4**, 124701 (2019).
[23] H. Sadeghi, M. Oberlack, and M. Gauding, J. Fluid Mech. **919**, A5 (2021).
[24] S. S. Girimaji and S. B. Pope, Phys. Fluids **2**, 242 (1990).
[25] M. Chertkov, A. Pumir, and B. I. Shraiman, Phys. Fluids **11**, 2394 (1999).
[26] L. Chevillard and C. Meneveau, Phys. Rev. Lett. **97**, 174501 (2006).
[27] E. Jeong and S. S. Girimaji, Theor. Comput. Fluid Dyn. **16**, 421 (2003).
[28] M. Wilczek and C. Meneveau, J. Fluid Mech. **756**, 191 (2014).
[29] P. L. Johnson and C. Meneveau, J. Fluid Mech. **804**, 387 (2016).
[30] R. M. Pereira, L. Moriconi, and L. Chevillard, J. Fluid Mech. **839**, 430 (2018).
[31] M. Gonzalez, Phys. Fluids **21**, 055104 (2009).
[32] T. Hater, H. Homann, and R. Grauer, Phys. Rev. E **83**, 017302 (2011).
[33] V. Gurarie and A. Migdal, Phys. Rev. E **54**, 4908 (1996).
[34] G. Falkovich, I. Kolokolov, V. Lebedev, and A. Migdal, Phys. Rev. E **54**, 4896 (1996).
[35] T. Grafke, R. Grauer, and S. Schindel, Commun. Comput. Phys. **18**, 577 (2015).
[36] M. I. Freidlin and A. D. Wentzell, *Random Perturbations of Dynamical Systems* (Springer, Berlin, 2012).
[37] A. Dembo and O. Zeitouni, *Large Deviations Techniques and Applications* (Springer-Verlag, Berlin, 2010).
[38] E. Balkovsky, G. Falkovich, I. Kolokolov, and V. Lebedev, Phys. Rev. Lett. **78**, 1452 (1997).
[39] T. Grafke, R. Grauer, T. Schäfer, and E. Vanden-Eijnden, Multiscale Model. Simul. **12**, 566 (2014).
[40] T. Grafke, R. Grauer, and T. Schäfer, J. Phys. A: Math. Theor. **48**, 333001 (2015).
[41] J. Laurie and F. Bouchet, New J. Phys. **17**, 015009 (2015).
[42] G. Dematteis, T. Grafke, M. Onorato, and E. Vanden-Eijnden, Phys. Rev. X **9**, 041057 (2019).
[43] S. Tong, E. Vanden-Eijnden, and G. Stadler, Commun. Appl. Math. Comput. Sci. **16**, 181 (2021).
[44] M. Alqahtani and T. Grafke, J. Phys. A: Math. Theor. **54**, 175001 (2021).
[45] L. Chevillard, C. Meneveau, L. Biferale, and F. Toschi, Phys. Fluids **20**, 101504 (2008).
[46] M. M. Afonso and C. Meneveau, Physica D **239**, 1241 (2010).
[47] L. Moriconi, R. M. Pereira, and L. S. Grigorio, J. Stat. Mech.: Theory Exp. (2014) P10015.
[48] S. Tang, R. Antonia, L. Djenidi, L. Danaila, and Y. Zhou, J. Fluid Mech. **847**, 244 (2018).
[49] K. R. Sreenivasan and R. Antonia, Annu. Rev. Fluid Mech. **29**, 435 (1997).
[50] R. M. Kerr, J. Fluid Mech. **153**, 31 (1985).
[51] C. Tong and Z. Warhaft, Phys. Fluids **6**, 2165 (1994).
[52] K. R. Sreenivasan, Proc. Roy. Soc. London A: Math. Phys. Sci. **434**, 165 (1991).
[53] L. S. Grigorio, F. Bouchet, R. M. Pereira, and L. Chevillard, J. Phys. A: Math. Theor. **50**, 055501 (2017).
[54] L. S. Grigorio, J. Phys. A: Math. Theor. **53**, 445001 (2020).
[55] L. H. Ryder, *Quantum Field Theory* (Cambridge University Press, Cambridge, UK, 1996).
[56] Z. F. Ezawa, *Quantum Hall Effects: Field Theoretical Approach and Related Topics* (World Scientific, Singapore, 2008).
[57] T. Schorlepp, T. Grafke, S. May, and R. Grauer, Philos. Trans. Royal Soc. A **380**, 20210051 (2022).
[58] J. Martın, C. Dopazo, and L. Valiño, Phys. Fluids **10**, 2012 (1998).
[59] S. R. S. Varadhan, Commun. Pure Appl. Math. **19**, 261 (1966).
[60] A. I. Chernykh and M. G. Stepanov, Phys. Rev. E **64**, 026306 (2001).

[61] G. B. Apolinário, L. Moriconi, and R. M. Pereira, Phys. Rev. E **99**, 033104 (2019).
[62] P. C. Martin, E. D. Siggia, and H. A. Rose, Phys. Rev. A **8**, 423 (1973).
[63] H.-K. Janssen, Z. Phys. B **23**, 377 (1976).
[64] C. de Dominicis, J. Phys. C **37**, C1-247 (1976).
[65] T. Grafke, R. Grauer, and T. Schäfer, J. Phys. A: Math. Theor. **46**, 062002 (2013).
[66] T. Grafke and E. Vanden-Eijnden, Chaos **29**, 063118 (2019).
[67] F. Rindler, *Calculus of Variations* (Springer, Berlin, 2018).
[68] W. T. Ashurst, A. Kerstein, R. Kerr, and C. Gibson, Phys. Fluids **30**, 2343 (1987).
[69] G. Gulitski, M. Kholmyansky, W. Kinzelbach, B. Lüthi, A. Tsinober, and S. Yorish, J. Fluid Mech. **589**, 83 (2007).